

CrossMark  
click for updatesCite this: *J. Mater. Chem. A*, 2016, 4, 17018

## Constructing water-resistant $\text{CH}_3\text{NH}_3\text{PbI}_3$ perovskite films *via* coordination interaction†

Bo Li,<sup>a</sup> Chengbin Fei,<sup>b</sup> Kaibo Zheng,<sup>ce</sup> Xuanhui Qu,<sup>a</sup> Tönu Pullerits,<sup>c</sup> Guozhong Cao<sup>ad</sup> and Jianjun Tian<sup>\*a</sup>

Organic–inorganic halide  $\text{CH}_3\text{NH}_3\text{PbI}_3$  (MAPbI<sub>3</sub>) perovskite solar cells (PSCs) have attracted intensive attention due to their high power conversion efficiency and low fabrication cost. However, MAPbI<sub>3</sub> is known to be very sensitive to humidity, and the intrinsic long-term stability of the MAPbI<sub>3</sub> film remains a critical challenge. 2-Aminoethanethiol (2-AET) was used as a ligand to bridge the organic compound (MAI) and inorganic compound (PbI<sub>2</sub>), which restricted the fast growth of PbI<sub>2</sub> to realize the synchronous growth environment of MAI and PbI<sub>2</sub> crystals, resulting in the formation of a compact MAPbI<sub>3</sub> film with polygonal grains. Due to the compact (PbI<sub>2</sub>)–2-AET–(MAI) molecule barrier layers in the MAPbI<sub>3</sub> structure, the resulting perovskite films showed excellent intrinsic water-resistance, with the MAPbI<sub>3</sub> perovskite crystal structure retained for a long time (>10 minutes) after immersion in water. This work makes a step towards obtaining long-term stable MAPbI<sub>3</sub> perovskite devices.

Received 12th August 2016  
Accepted 28th September 2016

DOI: 10.1039/c6ta06892h

www.rsc.org/MaterialsA

### Introduction

Methylammonium lead halide organic–inorganic hybrid perovskites, such as  $\text{CH}_3\text{NH}_3\text{PbI}_3$  (MAPbI<sub>3</sub>), have recently attracted enormous attention for thin-film solar cells due to their high optical absorption coefficient, long free carrier diffusion length, low exciton binding energy and simple low temperature solution-based processing.<sup>1–4</sup> Such organic–inorganic hybrid perovskite materials were first made several decades ago, the unique structure of the organic–inorganic perovskites show the potential applications in the electrical and optical fields.<sup>5–9</sup> To date, the highest power conversion efficiencies (PCEs) of the perovskite solar cells (PSCs) are above 21%,<sup>10</sup> approaching the record efficiencies of monocrystalline silicon-based solar cells (25.6%) and thin film single-crystalline GaAs cells (28.8%).<sup>11,12</sup> A serious current deficiency of PSCs is the high sensitivity of MAPbI<sub>3</sub> to humidity. The PCE drops nearly 90% under an ambient environment ( $T = 25^\circ\text{C}$ , 30–50% humidity) in a few days.<sup>13</sup> It has been shown that MAPbI<sub>3</sub> can be easily degraded to MAI, PbI<sub>2</sub>, and HI in a few hours under a high

humidity environment.<sup>14,15</sup> Moisture in air is considered a key factor causing the decomposition of MAPbI<sub>3</sub>. Compared to monocrystalline silicon-based solar cells with 20–30 years guaranteed lifetime, the poor stability of PSCs is a crucial barrier to their practical applicability.

Moisture stability has become one of the focus areas of MAPbI<sub>3</sub> research. For example, the surfaces of devices or perovskite were covered by p-type metal oxides, hydrophobic materials or insulating polymers to enhance the stability of PSCs under an ambient atmosphere.<sup>13,16,17</sup> However, the intrinsic water sensitivity of perovskite films remains an unsolved problem. Recently, it was demonstrated that hydrate intermediate compounds, such as  $\text{MAPbI}_3 \cdot \text{H}_2\text{O}$  and  $(\text{MA})_4\text{-PbI}_6 \cdot 2\text{H}_2\text{O}$ , were formed at the initial stage of the MAPbI<sub>3</sub> decomposition process under controlled humidity conditions, and the degradation reaction could be reversed by drying treatment.<sup>18–20</sup> In MAPbI<sub>3</sub> perovskite crystals, inorganic PbI<sub>2</sub> frameworks and organic MA<sup>+</sup> cations are bound together by weak hydrogen and ionic bonds. The migration activation energy for MA<sup>+</sup> is approximately 0.84 eV, determined by first-principles calculations.<sup>21–23</sup> The strength of hydrogen bonding will be reduced when the perovskite crystal is exposed to H<sub>2</sub>O or other polar solvents, and MA<sup>+</sup> would readily separate from octahedral PbI<sub>6</sub>, resulting in a rapid decomposition of MAPbI<sub>3</sub> and degradation of solar cell performance. It has been suggested that chemical modification between organic cation MA<sup>+</sup> and inorganic framework PbI<sub>6</sub> in MAPbI<sub>3</sub> perovskite can be a way to achieve inherent moisture stability.<sup>24–26</sup> For example, butylphosphonic acid 4-ammonium chloride was chosen to crosslink neighboring perovskite grains through hydrogen bonding, leading to increased photovoltaic performance and

<sup>a</sup>Institute of Advanced Materials and Technology, University of Science and Technology Beijing, 100083, China. E-mail: tianjianjun@mater.ustb.edu.cn

<sup>b</sup>Beijing Institute of Nanoenergy and Nanosystems, Chinese Academy of Sciences, 100083, China

<sup>c</sup>Department of Chemical Physics and NanoLund, Lund University, Box 124, 22100 Lund, Sweden

<sup>d</sup>Department of Materials and Engineering, University of Washington, Seattle, WA 98195-2120, USA

<sup>e</sup>Gas Processing Center, Department of Chemical Engineering, Qatar University, Qatar

† Electronic supplementary information (ESI) available. See DOI: 10.1039/c6ta06892h



moisture stability.<sup>24</sup> 2-Aminoethanethiol (2-AET) has been extensively used as a bidentate chelating agent in coordination chemistry, and shows a high affinity toward binding to Pb<sup>2+</sup> through the thiolate group.<sup>27–31</sup> In addition, the ammonium group in 2-AET molecules would bind MAI by hydrogen bonds in the perovskite structure. Therefore, 2-AET can be a great ligand to improve the intrinsic long-term stability of MAPbI<sub>3</sub> perovskite.

The present paper reports the fabrication of a novel water-resistant MAPbI<sub>3</sub>·2-AET perovskite film, with the MAPbI<sub>3</sub> crystal structure retained after immersion in water at room temperature (RT) for a long time (>10 minutes). When 2-AET was added into perovskite precursor solution, the thiolate group of 2-AET molecules facilitates strong interaction with PbI<sub>2</sub>, while the ammonium group can anchor MAI to form PbI<sub>2</sub>·2-AET·MAI when DMF is removed, providing a homogeneous environment for perovskite crystal nucleation and growth, and leading to uniform perovskite films with excellent crystallinity.

## Experimental section

### Materials synthesis and perovskite film fabrication

CH<sub>3</sub>NH<sub>2</sub>I (MAI) was prepared by the reported method.<sup>32</sup> Methylamine (33 wt% in methanol) was mixed with hydroiodic acid (HI, 57 wt%) in a molar ratio of 1.2 : 1 at 0 °C. After stirring for 2 h under a N<sub>2</sub> atmosphere, the solvent was removed by using a rotary evaporator at 50 °C. Then the obtained powder was washed with ethyl acetate (EA) three times, and then recrystallized in methanol. Finally, the product powder was dried at 60 °C in a vacuum oven for 24 h.

The standard perovskite precursor solutions were prepared by sequentially dissolving the synthesized 159 mg MAI powder and 462 mg PbI<sub>2</sub> (Yingkou You Xuan Trade Co., LTD) in 1 mL *N,N*-dimethylformamide (DMF, 99.8%, Sigma-Aldrich).<sup>33</sup> 2-Aminoethanethiol (2-AET, 95%, Adamas Regent, Ltd.) was added into the perovskite precursor solutions. The precursor solutions were filtered by using a 0.22 μm pore PVDF syringe filter before spin coating.

45 μL standard perovskite precursor solution was spin coated onto FTO substrates at 3500 rpm for 20 s and 5000 rpm for 10 s, followed by annealing at 100 °C for 10 min.

A MAI·2-AET complex was obtained by adding 3 mL ethyl acetate into 1 mL MAI/2-AET (1 : 1 mol%) DMF solution, and the solid complex was filtered and dried at 60 °C in a vacuum oven for 3 h. The MAI/PbI<sub>2</sub> complex was obtained by adding 3 mL ethyl acetate into perovskite precursor solution (1 : 1 mol%), and the solid complex was filtered and dried at 60 °C in a vacuum oven for 3 h. The MAI·2-AET·PbI<sub>2</sub> complex was obtained by adding 3 mL ethyl acetate into 1 mL 2-AET added perovskite precursor solution (1 : 1 : 1 mol%), and the solid complex was filtered and dried at 60 °C in a vacuum oven for 3 h.

### Characterization

The IR spectra were measured by using a Bruker Vertex 80v Fourier transform infrared (FTIR) spectrometer. The scanning electron microscopy (SEM) measurements were performed

using a cold field emission scanning electron microscope (SU8020, Hitachi). The crystal structure was analyzed by using an X-ray diffractometer (PANalytical, Netherlands) with a monochromatic Cu K $\alpha$  radiation source ( $\lambda = 1.54056 \text{ \AA}$ ). The absorption spectra were recorded using an ultraviolet-visible (UV-vis) spectrophotometer (UV-3600, Shi-madzu). The photoluminescence (PL) spectra were measured using a steady state fluorescence spectrometer (FLS980, Edinburgh), and the excitation wavelength was 465 nm. The weight loss was measured on a TGA/DSC instrument (STA 4493F3, NETZSCH) from 30–350 °C with a heating rate of 5 °C min<sup>-1</sup>.

## Results and discussion

Fig. 1(a) shows the chemical structures of MAI, PbI<sub>2</sub> and 2-AET; the 2-AET molecule contains thiolate and ammonium functional groups. In order to completely dissolve PbI<sub>2</sub> in DMF solvent, a heating process at 70 °C was usually needed due to the weak interaction of Pb–O coordination bonds between PbI<sub>2</sub> and DMF.<sup>34–38</sup> However, as shown in Fig. S1,† PbI<sub>2</sub> was quickly dissolved in DMF when 0.2 M 2-AET was added into DMF solution at RT. Fig. 1(b) shows the Fourier transform infrared (FTIR) spectra of pure DMF, PbI<sub>2</sub> and PbI<sub>2</sub>/2-AET DMF solution. The stretching vibration of the C=O bond appears at 1660 cm<sup>-1</sup> for pure DMF, which is shifted to 1633 cm<sup>-1</sup> for PbI<sub>2</sub> DMF solution, and then the shoulder on the shorter wavenumber side disappears when 2-AET is added into PbI<sub>2</sub> solution. Considering that the interaction between Pb–S coordination bonds is stronger than that between Pb–O coordination bonds,<sup>39–41</sup> the Pb–O coordination bond is replaced by the Pb–S coordination bond when 2-AET is added into PbI<sub>2</sub> DMF solution. It demonstrates that the strong interaction of the Pb–S coordination bond between PbI<sub>2</sub> and 2-AET is formed in PbI<sub>2</sub> DMF solution. Fig. S2† shows FTIR spectra of MAI and MAI/2-AET DMF

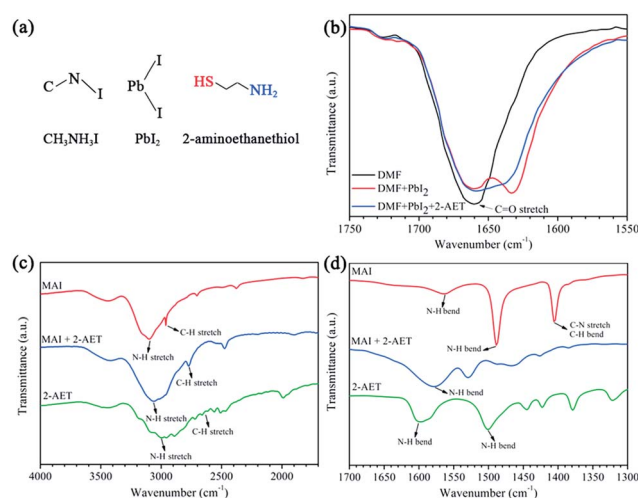


Fig. 1 Chemical structures (a) of MAI, PbI<sub>2</sub> and 2-AET; FTIR spectra of pure DMF, PbI<sub>2</sub> DMF solution and 2-AET/PbI<sub>2</sub> DMF solution in the range of 1750–1550 cm<sup>-1</sup> (b); FTIR spectra of MAI, 2-AET and MAI·2-AET solid complexes in the range of 4000–1700 cm<sup>-1</sup> (c) and 1700–1300 cm<sup>-1</sup> (d).



solution, and there is no obvious peak shift, which implies that the interaction between MAI and 2-AET is not formed in DMF solution. In order to further understand the effect of 2-AET on the interaction among  $\text{PbI}_2$ , MAI and DMF, the solid complexes were extracted from the precursor solution with ethyl acetate (EA) as an extraction agent. Fig. S3(a)† shows the complex without 2-AET dividing into a white upper layer and a yellow bottom layer. The white and yellow products are MAI and  $\text{PbI}_2$ , respectively. It demonstrates that there is weak interaction among  $\text{PbI}_2$ , MAI and DMF. No separated layers in the small volume of yellow complexes are found when 2-AET is added into the precursor solution. The complex is fluid, indicating that the strong interaction among  $\text{PbI}_2$ , MAI and 2-AET is formed after extraction. Fig. S3(b)† shows the Tyndall effect in the complex with the addition of 2-AET under red light illumination, indicating the colloidal characteristic of the complex. Fig. 1(c) and (d) show FTIR spectra of MAI, 2-AET and MAI·2-AET solid complexes. The N–H bending vibration and N–H stretching vibration appear at  $1597\text{ cm}^{-1}$  and  $2989\text{ cm}^{-1}$  for 2-AET, and at  $1564\text{ cm}^{-1}$  and  $3099\text{ cm}^{-1}$  for MAI. However, the N–H bending vibration and N–H stretching vibration of the MAI·2-AET complex shift to  $1578\text{ cm}^{-1}$  and  $3059\text{ cm}^{-1}$ , respectively. The N–H vibration frequency of the MAI·2-AET complex is between the 2-AET and MAI, providing evidence for interaction between 2-AET and MAI. Fig. S3(c) and (d)† show X-ray diffraction (XRD) patterns of the complexes with and without the additive of 2-AET. It can be seen that the diffraction peaks could not be indexed to MAI,  $\text{PbI}_2$  or  $\text{MAPbI}_3$  for the complex without 2-AET, as reported in the literature.<sup>42</sup> XRD patterns of the complex with the addition of 2-AET show several peaks of the new intermediate phase, due to the coordination interaction of 2-AET. Notably, the color of the solid complex without 2-AET changes from yellow to black at the edge after measurement, but the solid complex with the 2-AET sample remains yellow, which implies that 2-AET can retard the change of the intermediate phase to the  $\text{MAPbI}_3$  phase at RT. The intermediate phases changed to the  $\text{MAPbI}_3$  phase when the complexes were annealed at  $100\text{ }^\circ\text{C}$  for 30 min in air. The thiolate group in 2-AET can interact with  $\text{PbI}_2$  to form a  $\text{PbI}_2\cdot 2\text{-AET}$  complex in 2-AET added perovskite precursor solution, while the ammonium group can anchor MAI to form  $\text{PbI}_2\cdot 2\text{-AET}\cdot\text{MAI}$  when DMF is removed.

The scanning electron microscopy (SEM) images, XRD patterns and statistical grain size distribution of final  $\text{MAPbI}_3\cdot(x)\text{2-AET}$  perovskite films are illustrated in Fig. 2. In the case of the perovskite film without 2-AET, it clearly shows the typical branch-like perovskite grains with poor coverage on the FTO substrate, which is in accordance with the literature.<sup>43,44</sup> The morphology of  $\text{MAPbI}_3$  perovskite is usually related to the reaction rate between  $\text{PbI}_2$  and MAI, which depends on their respective solubility and diffusivity in precursor solution.<sup>41,45,46</sup> Due to the good crystallinity and poor solubility of  $\text{PbI}_2$  in precursor solution,<sup>35</sup>  $\text{PbI}_2$  crystals first precipitate out to form an inorganic framework during the spin coating process, and then react with MAI to form  $\text{MAPbI}_3$  crystals. So the  $\text{MAPbI}_3$  crystallization process is dominated by the crystallization rate of  $\text{PbI}_2$ . The asynchronous reaction for  $\text{PbI}_2$  and MAI is likely to lead to the growth of branch-like

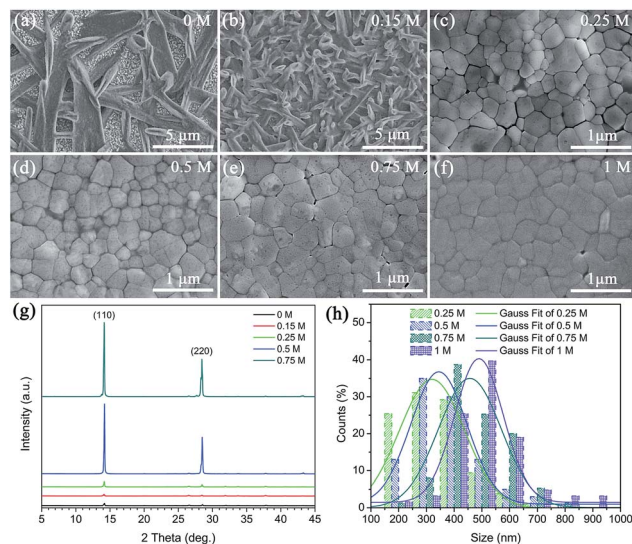


Fig. 2 SEM images of  $\text{MAPbI}_3\cdot(x)\text{2-AET}$  perovskite films prepared on FTO substrates, (a)  $x = 0$ ; (b)  $x = 0.15\text{ M}$ ; (c)  $x = 0.25\text{ M}$ ; (d)  $x = 0.5\text{ M}$ ; (e)  $x = 0.75\text{ M}$ ; (f)  $x = 1\text{ M}$ . XRD patterns (g) and statistical grain size distribution (h) of  $\text{MAPbI}_3\cdot(x)\text{2-AET}$  perovskite films.

crystals of  $\text{MAPbI}_3$ . Retarding the crystallization rate of  $\text{PbI}_2$  is considered an efficient method to obtain uniaxial grains for high performance of PSCs.<sup>38,41</sup> As shown in Fig. 2(b)–(f), the addition of 2-AET has changed the morphology, surface coverage and roughness of the perovskite films. The  $\text{MAPbI}_3$  film consists of compact polygonal perovskite grains when 0.25 M 2-AET is added into the precursor solution. The average size of perovskite grains increases with increasing the addition of 2-AET. As shown in Fig. 2(h), the average grain size is determined to be  $\sim 320\text{ nm}$  for 0.25 M,  $\sim 350\text{ nm}$  for 0.5 M,  $\sim 460\text{ nm}$  for 0.75 M and  $\sim 490\text{ nm}$  for 1 M. The addition of 2-AET reduces the crystallization rate of  $\text{PbI}_2$ , which makes the crystallization synchronization of  $\text{PbI}_2$  and  $\text{MAPbI}_3$  form polygonal grains. Fig. 2(g) shows XRD patterns of final  $\text{MAPbI}_3\cdot(x)\text{2-AET}$  perovskite films. Diffraction peaks at  $14.14^\circ$  and  $28.45^\circ$  are the only peaks and correspond to (110) and (220) crystal planes of the  $\text{MAPbI}_3$  perovskite structure,<sup>47,48</sup> and revealed significantly preferred orientation with increasing the addition of 2-AET. The diffraction intensity of the perovskite films with 0.5 M and 0.75 M 2-AET increases by an order of magnitude as compared with the perovskite film without 2-AET, which implied better crystallinity of  $\text{MAPbI}_3\cdot(x)\text{2-AET}$  perovskite films. No obvious position shift of diffraction peaks is observed. A uniform and compact perovskite film with excellent crystallinity is one of the essential requirements for PSC application.<sup>45–47,49</sup>

The effect of thermal treatment on the  $\text{MAPbI}_3$  perovskite films was investigated. Fig. 3(a)–(f) show SEM images of  $\text{MAPbI}_3\cdot(0.5)\text{2-AET}$  perovskite films heated at  $100\text{ }^\circ\text{C}$  for different times. There are many pinholes in the  $\text{MAPbI}_3$  film without annealing. With the increase of annealing time, perovskite grains grow up and decrease the pinholes. The average grain size of the  $\text{MAPbI}_3$  grows up to  $\sim 490\text{ nm}$  after annealing at  $100\text{ }^\circ\text{C}$  for 12 min. So the compact perovskite films are obtained. 2-AET also boosts the growth rate of perovskite crystals during annealing. Fig. S4† shows that the surface



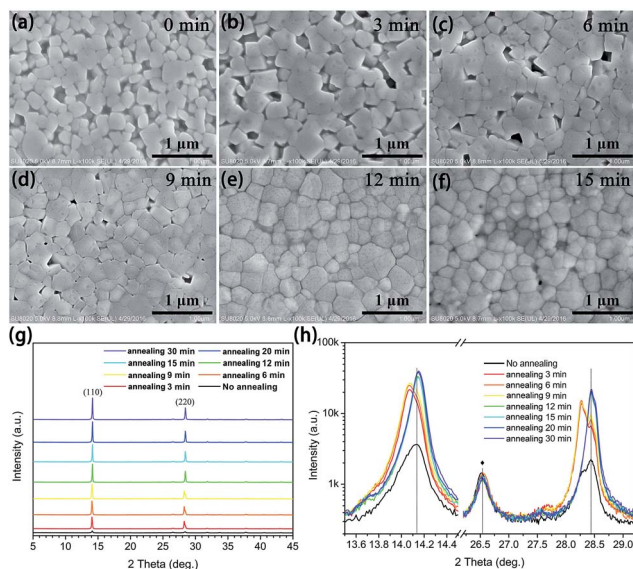


Fig. 3 SEM images of  $\text{MAPbI}_3 \cdot (0.5)2\text{-AET}$  perovskite films with different thermal annealing times at  $100^\circ\text{C}$ . (a) 0 min; (b) 3 min; (c) 6 min; (d) 9 min; (e) 12 min; (f) 15 min. XRD patterns (g) of  $\text{MAPbI}_3 \cdot (0.5)2\text{-AET}$  perovskite films with different thermal annealing times at  $100^\circ\text{C}$  prepared on FTO substrates; selected ranges (h) which contain characteristic diffraction peaks at  $13.5\text{--}14.5^\circ$  and  $27\text{--}29^\circ$ . The diamond indicates the FTO diffraction peaks at  $26.52^\circ$ .

coverage of the  $\text{MAPbI}_3 \cdot (0.75)2\text{-AET}$  perovskite film is higher than that of the  $\text{MAPbI}_3 \cdot (0.5)2\text{-AET}$  perovskite film after annealing, indicating that the growth rate of perovskite is accelerated by 2-AET. Fig. 3(g) and (h) show XRD patterns of  $\text{MAPbI}_3$  perovskite films after thermal annealing at  $100^\circ\text{C}$  for different durations. All annealed perovskite films present increased intensity of diffraction peaks of (110) and (220) crystal planes of the  $\text{MAPbI}_3$  perovskite structure at  $14.14^\circ$  and  $28.45^\circ$ . There is no detectable peak in the films with increasing the duration of thermal annealing. Table S1† shows the decreased full width at half maximum (FWHM) from 0.22 to 0.11, demonstrating the increased crystallinity of perovskite with increased annealing time. The characteristic peaks of the perovskite films are found to shift to lower angles after annealing for 3 min, and then shift back to higher angles after annealing for 12 min. The reason is ascribed to the effect of 2-AET in the  $\text{MAPbI}_3$  structure. For  $\text{MAPbI}_3 \cdot (0.5)2\text{-AET}$ , a part of the free  $\text{PbI}_2$  and MAI change to  $\text{MAPbI}_3$  after spin coating. The initially formed film has a poor crystallinity and weak optical absorption of  $\text{MAPbI}_3$  as shown in Table S1 and Fig. S5.† During the annealing process, the 2-AET additive was gradually pushed out to the boundaries of perovskite grains, which increased the perovskite crystal plane spacing. Subsequently, perovskite grains grew up, which tended to gradually decrease the crystal plane spacing.

Fig. 4 is the schematic illustration of the crystallization process of  $\text{MAPbI}_3$ . The branch-like crystals of  $\text{MAPbI}_3$  are obtained from standard precursor solution *via* the asynchronous reaction between  $\text{PbI}_2$  and MAI. When 2-AET is added into the standard precursor solution, the  $\text{PbI}_2 \cdot 2\text{-AET}$  coordination

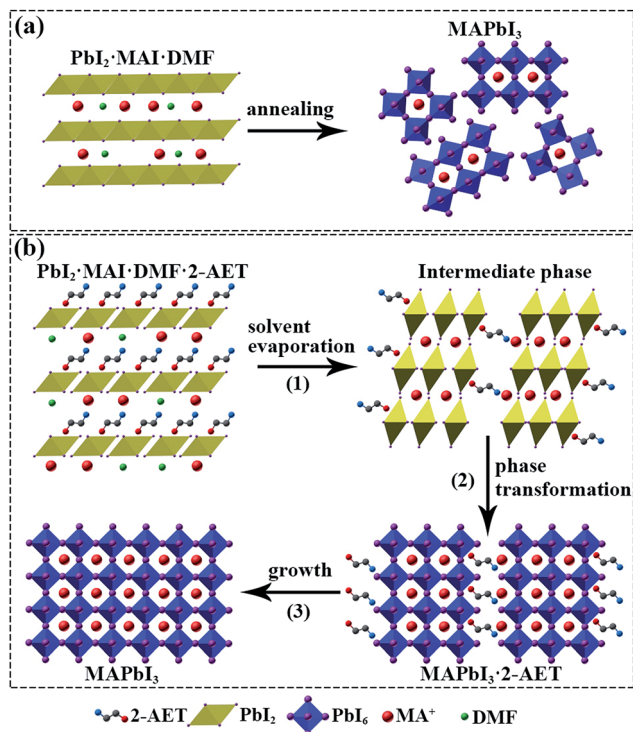


Fig. 4 Schematic illustration of crystallographic conversion during the annealing process. (a) Without the 2-AET additive and (b) with the 2-AET additive.

complex is formed to retard the fast crystallization of  $\text{PbI}_2$ . After spin coating at RT, the  $\text{PbI}_2 \cdot \text{MAI} \cdot \text{DMF} \cdot 2\text{-AET}$  films are obtained, which provide the synchronous growth environment of MAI and  $\text{PbI}_2$  crystals. There are three stages to finish the crystallization of perovskite crystals during the annealing process. The remnant DMF gradually evaporates and the  $\text{MAPbI}_3 \cdot \text{PbI}_2 \cdot \text{MAI} \cdot 2\text{-AET}$  intermediate phase is formed during the annealing stage (1). Then the intermediate phases obtain enough thermal energy to break the coordination interaction of 2-AET in the annealing stage (2), and the 2-AET additive is concentrated in the grain boundaries of perovskite grains. Finally, together with the growth process of perovskite grains, the 2-AET additive is driven from grain boundaries to the surface of perovskite grains in the stage (3) as shown in Fig. S4(d).†

Fig. 5(a) shows UV-vis absorbance of  $\text{MAPbI}_3$  perovskite films prepared with different additions of 2-AET. Without 2-AET, the shape of the spectrum shows clear evidence that the film does not provide perfect coverage and consists of areas of high optical density mixed with uncovered parts.<sup>50</sup> The perovskite film prepared with 0.15 M 2-AET shows less of this effect. Clearly, the higher concentration of M 2-AET leads to a high-quality film with close to perfect coverage. We point out that the absorption of perovskite films gradually drops when the addition is more than 0.25 M. It should be attributed to the strong coordination interaction of 2-AET in the perovskite film, which forms the complex in the final film, as indicated by the unknown XRD peaks in Fig. S6.† Besides, the decrease of the



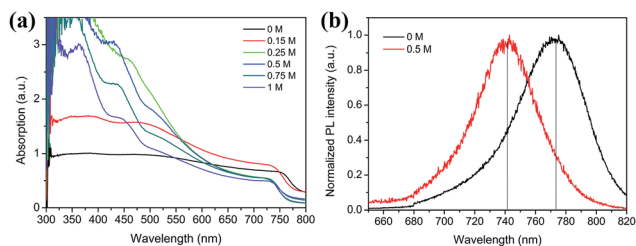


Fig. 5 UV-vis absorption spectra (a) and normalized steady-state photoluminescence (PL) spectra (b) of  $\text{MAPbI}_3 \cdot (x)2\text{-AET}$  perovskite films. The excitation wavelength is 465 nm.

absorption of the perovskite films in the 775–800 nm region is caused by the reduced light scattering. The weak light scattering for 2-AET added perovskite films is attributed to the uniform morphology. UV-vis absorption spectra also show a blue shift by  $\sim 30$  nm from  $\text{MAPbI}_3$  to  $\text{MAPbI}_3 \cdot (0.25)2\text{-AET}$ , which is another evidence for the interaction between  $\text{PbI}_2$ , MAI and 2-AET. The steady-state photoluminescence (PL) spectra in Fig. 5(b) show that the peak of the  $\text{MAPbI}_3 \cdot (0.5)2\text{-AET}$  perovskite film is blue shifted by  $\sim 30$  nm compared to  $\text{MAPbI}_3$  perovskite.

Fig. 6(a) and (b) show the photographs of  $\text{MAPbI}_3$  and  $\text{MAPbI}_3 \cdot (0.5)2\text{-AET}$  perovskite films immersed in water for different times at RT. SEM images of the films are shown in Fig. S7 and S8.† It can be seen that the color of  $\text{MAPbI}_3 \cdot (0.5)2\text{-AET}$  perovskite films remains dark brown after immersion in

water, while  $\text{MAPbI}_3$  perovskite films undergo a rapid color change from dark brown to yellow. This process has also been recorded in Movie S1.† XRD patterns of  $\text{MAPbI}_3$  and  $\text{MAPbI}_3 \cdot (0.5)2\text{-AET}$  are shown in Fig. 6(c) and (d). For  $\text{MAPbI}_3$  perovskite films,  $\text{PbI}_2$  characteristic peaks at  $12.7^\circ$ ,  $25.9^\circ$ , and  $34.3^\circ$  appear after immersion in water for 10 s, and are well indexed to hexagonal  $\text{PbI}_2$  (JCPDS card no. 07-0235). For  $\text{MAPbI}_3 \cdot (0.5)2\text{-AET}$  perovskite films, characteristic peaks at  $14.15^\circ$  and  $28.46^\circ$  of  $\text{MAPbI}_3$  remain after immersion in water from 10 s to 300 s, without the presence of detectable crystalline  $\text{PbI}_2$ . However, the intensity of the peaks decreases gradually with increasing immersion time from 10 s to 300 s. No visible diffraction peak offset nor impurity peaks were observed. Compared to the pristine  $\text{MAPbI}_3 \cdot (0.5)2\text{-AET}$  perovskite film, the UV-vis absorption of the film is first enhanced in the wavelength range from 450 nm to 800 nm after immersion in water for 10 s as shown in Fig. 6(e). The possible reason is that the excess 2-AET in the perovskite grain boundary is gradually dissolved in water to form holes in the perovskite film (as shown in Fig. S8†), which enhances the light trapping and the light scattering. Then the absorption is gradually decreased in the short wavelength range with increasing immersion time. However, the absorption edge of  $\text{PbI}_2$  at  $\sim 520$  nm as reported in the literature is not found.<sup>51</sup> A red shift of the absorption edge from  $\sim 770$  nm to  $\sim 780$  nm was also observed for all  $\text{MAPbI}_3 \cdot (0.5)2\text{-AET}$  perovskite films after immersion due to the light scattering. As shown in Fig. 6(f), after immersion, the PL peaks also shift 10 nm from 742 nm to 752 nm. After that, the PL curves do not change with increasing immersion time, indicating that the structure of  $\text{MAPbI}_3 \cdot (0.5)2\text{-AET}$  is stable in water.

Fig. 7(a) shows XRD patterns of  $\text{MAPbI}_3$  perovskite films prepared with low addition of 2-AET after immersion in water for 15 s. The degradation rate of  $\text{MAPbI}_3 \cdot (x)2\text{-AET}$  increases as the amount of 2-AET addition decreases. As shown in Table S2,† after immersion in water for 15 s, the diffraction peak of  $\text{PbI}_2$  at  $12.79^\circ$  shifts to  $12.22^\circ$  when the addition of 2-AET increases from 0 M to 0.3 M. The decreased intensity with increased FWHM of  $\text{PbI}_2$  characteristic peaks implies that the  $\text{MAPbI}_3$  degradation process is suppressed by the presence of 2-AET. The schematic diagram of the degradation process of  $\text{MAPbI}_3$  and possible mechanism of water-resistant  $\text{MAPbI}_3 \cdot (x)2\text{-AET}$  perovskite in water are presented in Fig. 7(b) and (c). The

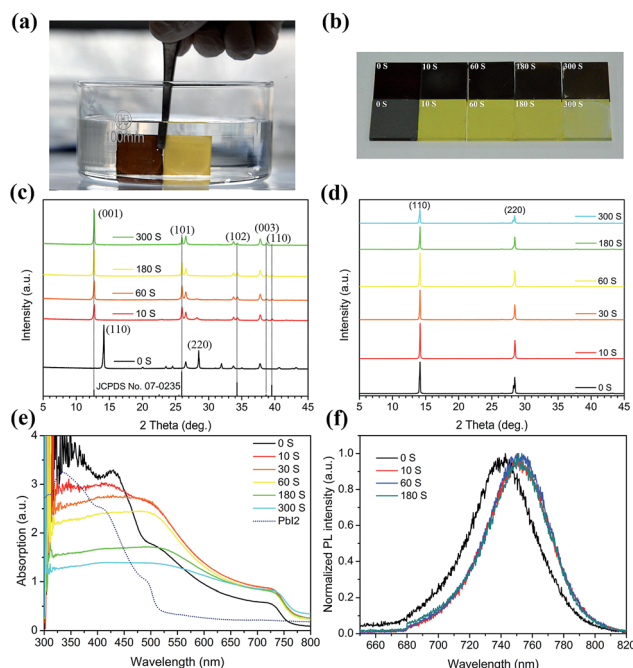


Fig. 6 Photographs (a and b) of  $\text{MAPbI}_3 \cdot (0.5)2\text{-AET}$  (top)  $\text{MAPbI}_3$  (bottom) perovskite films immersed in water at different times; XRD patterns of (c)  $\text{MAPbI}_3$  perovskite films and (d)  $\text{MAPbI}_3 \cdot (0.5)2\text{-AET}$  perovskite films immersed in water at different times. UV-vis absorption spectra (e) and normalized steady-state photoluminescence spectra (f) of  $\text{MAPbI}_3$  (black) and  $\text{MAPbI}_3 \cdot (0.5)2\text{-AET}$  (red) perovskite films immersed in water at different times, respectively. The excitation wavelength is 465 nm.

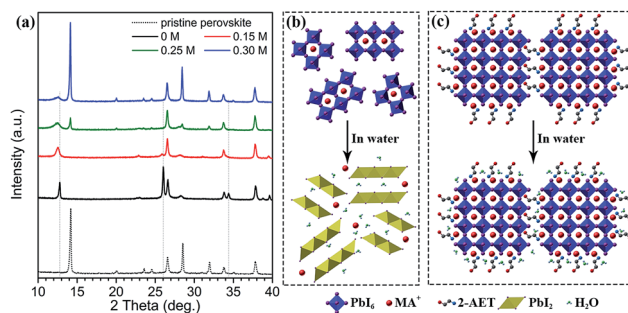


Fig. 7 XRD patterns (a) of  $\text{MAPbI}_3 \cdot (x)2\text{-AET}$  perovskite films immersed in water 15 s. Schematic diagram to show (b) the degradation process of  $\text{MAPbI}_3$  and (c) the mechanisms for water-resistant  $\text{MAPbI}_3 \cdot (x)2\text{-AET}$  perovskite in water.



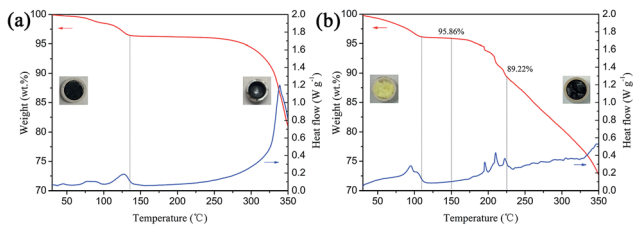


Fig. 8 DSC/TGA curves of MAPbI<sub>3</sub> (a) and MAPbI<sub>3</sub>·(0.75)2-AET (b) in the range of 30–350 °C at 5 °C min<sup>-1</sup> of heating rate. DSC curve (red line), TGA curve (blue line). The inset photographs are perovskite powders before (left) and after (right) measurement.

MAPbI<sub>3</sub> film prepared without the addition of 2-AET degrades rapidly to hexagonal PbI<sub>2</sub>. However, in the case of the MAPbI<sub>3</sub> film prepared with addition of 2-AET, the distribution of 2-AET in perovskite grain boundaries forms compact (PbI<sub>2</sub>)–2-AET–(MAI) molecule barrier layers, which can effectively prevent H<sub>2</sub>O from penetrating into MAPbI<sub>3</sub> crystals. As a result, although 2-AET dissolves easily in water, MAPbI<sub>3</sub>·(x)2-AET perovskite shows excellent water-resistance due to the coordination interaction between 2-AET and MAPbI<sub>3</sub> by hydrogen bonds.

Fig. 8 shows differential scanning calorimetry/thermogravimetric analysis (DSC/TGA) curves of MAPbI<sub>3</sub> and MAPbI<sub>3</sub>·(0.75)2-AET. The color of MAPbI<sub>3</sub>·(0.75)2-AET powders changed from yellow to black after the TGA/DSC measurement, while the color of MAPbI<sub>3</sub> still remained black. The weight loss for both perovskite powders is approximately the same, 4% from RT to 125 °C, which is attributed to the evaporation of physically adsorbed H<sub>2</sub>O or DMF. For MAPbI<sub>3</sub> powder, the TGA curve stepwise decreases with an obvious endothermic peak at ~125 °C, likely due to the removal of combined water.<sup>52</sup> In the case of MAPbI<sub>3</sub>·(0.75)2-AET powder, the mass consecutively drops with an increasing temperature from 30 °C to 125 °C, and there is no endothermic peak at ~125 °C, so the weight loss is related to evaporation of DMF. This may imply that the reported hydrate intermediate compounds (MAPbI<sub>3</sub>·H<sub>2</sub>O or (MA)<sub>4</sub>PbI<sub>6</sub>·2H<sub>2</sub>O) are not formed in MAPbI<sub>3</sub>·(0.75)2-AET powder.<sup>18–20</sup> No visible weight loss is observed between 125 °C and 225 °C for MAPbI<sub>3</sub> powder, which is consistent with other reports.<sup>52–54</sup> The weight loss is 6.64% between 150 °C and 225 °C for MAPbI<sub>3</sub>·(0.75)2-AET powder, which is close to the amount of (8.54%) 2-AET added into precursor solution. However, as shown in Fig. S9,† for pure 2-AET powder, the weight loss is only 6.27%. In addition, the DSC curve shows obvious endothermic peaks at 200–225 °C, so the poor thermal stability should be attributed to a series of reactions between MAPbI<sub>3</sub> and 2-AET, and the reaction products will be evaporated from the perovskite powder.

## Conclusions

Excellent and intrinsic water-resistant MAPbI<sub>3</sub>·(x)2-AET perovskite films have been grown and demonstrated. 2-AET is a ligand with strong coordination interactions not only observed in the perovskite precursor solutions, but also in the resulting perovskite crystal structure. The colloidal

PbI<sub>2</sub>·2-AET·MAI complexes have a great influence on the nucleation and growth process, and the synchronous growth of MAI and PbI<sub>2</sub> crystals is realized during a one step spin coating process. MAPbI<sub>3</sub>·(x)2-AET during the thermal annealing process leads to the growth of compact perovskite films with significant preferential orientation of (110) and (220) planes and enhanced crystallinity. Due to the compact (PbI<sub>2</sub>)–2-AET–(MAI) molecule barrier layers in the MAPbI<sub>3</sub> structure, the perovskite films show excellent intrinsic water-resistance, with the MAPbI<sub>3</sub> perovskite crystal structure retained after immersion in water for a long time (>10 minutes).

## Acknowledgements

This work was supported by the National Science Foundation of China (51374029 and 51611130063), Program for New Century Excellent Talents in University (NCET-13-0668), Fundamental Research Funds for the Central Universities (FRF-TP-14-008C1), NPRP grant from the Qatar National Research Fund (a member of Qatar Foundation) (# NPRP7-227-1-034) and STINT grant #CH2015-6232 from the Swedish Foundation for International Cooperation in Research and Higher Education.

## References

- 1 L. Etgar, P. Gao, Z. Xue, Q. Peng, A. K. Chandiran, B. Liu, M. K. Nazeeruddin and M. Gratzel, *J. Am. Chem. Soc.*, 2012, **134**, 17396–17399.
- 2 H. S. Kim, C. R. Lee, J. H. Im, K. B. Lee, T. Moehl, A. Marchioro, S. J. Moon, R. Humphry-Baker, J. H. Yum, J. E. Moser, M. Gratzel and N. G. Park, *Sci. Rep.*, 2012, **2**, 591.
- 3 G. Xing, N. Mathews, S. Sun, S. S. Lim, Y. M. Lam, M. Gratzel, S. Mhaisalkar and T. C. Sum, *Science*, 2013, **342**, 344–347.
- 4 V. D'Innocenzo, G. Grancini, M. J. Alcocer, A. R. Kandada, S. D. Stranks, M. M. Lee, G. Lanzani, H. J. Snaith and A. Petrozza, *Nat. Commun.*, 2014, **5**, 3586.
- 5 A. Poglitsch and D. Weber, *J. Chem. Phys.*, 1987, **87**, 6373–6378.
- 6 D. B. Mitzi, *Prog. Inorg. Chem.*, 1999, **48**, 1–121.
- 7 D. B. Mitzi, K. Chondroudis and C. R. Kagan, *IBM J. Res. Dev.*, 2001, **45**, 29–45.
- 8 D. Weber, *Z. Naturforsch., B: J. Chem. Sci.*, 1978, **33**, 1443–1445.
- 9 X. Qin, H. Dong and W. Hu, *Sci. China Mater.*, 2015, **58**, 186–191.
- 10 M. Saliba, T. Matsui, J.-Y. Seo, K. Domanski, J.-P. Correa-Baena, M. K. Nazeeruddin, S. M. Zakeeruddin, W. Tress, A. Abate, A. Hagfeldt and M. Grätzel, *Energy Environ. Sci.*, 2016, **9**, 1989–1997.
- 11 M. A. Green, K. Emery, Y. Hishikawa, W. Warta and E. D. Dunlop, *Prog. Photovoltaics*, 2015, **23**, 1–9.
- 12 A. Polman, M. Knight, E. C. Garnett, B. Ehrler and W. C. Sinke, *Science*, 2016, **352**, aad4424.
- 13 J. You, L. Meng, T. B. Song, T. F. Guo, Y. M. Yang, W. H. Chang, Z. Hong, H. Chen, H. Zhou, Q. Chen, Y. Liu, N. De Marco and Y. Yang, *Nat. Nanotechnol.*, 2016, **11**, 75–81.



- 14 G. Niu, W. Li, F. Meng, L. Wang, H. Dong and Y. Qiu, *J. Mater. Chem. A*, 2014, **2**, 705–710.
- 15 J. M. Frost, K. T. Butler, F. Brivio, C. H. Hendon, M. van Schilfhaarde and A. Walsh, *Nano Lett.*, 2014, **14**, 2584–2590.
- 16 I. Hwang, I. Jeong, J. Lee, M. J. Ko and K. Yong, *ACS Appl. Mater. Interfaces*, 2015, **7**, 17330–17336.
- 17 Q. Wang, Q. Dong, T. Li, A. Gruverman and J. Huang, *Adv. Mater.*, 2016, 1–6.
- 18 J. Yang, B. D. Siempelkamp, D. Liu and T. L. Kelly, *ACS Nano*, 2015, **9**, 1955–1963.
- 19 A. M. A. Leguy, Y. Hu, M. Campoy-Quiles, M. I. Alonso, O. J. Weber, P. Azarhoosh, M. van Schilfhaarde, M. T. Weller, T. Bein, J. Nelson, P. Docampo and P. R. F. Barnes, *Chem. Mater.*, 2015, **27**, 3397–3407.
- 20 J. A. Christians, P. A. Miranda Herrera and P. V. Kamat, *J. Am. Chem. Soc.*, 2015, **137**, 1530–1538.
- 21 D. B. Mitzi, *J. Mater. Chem.*, 2004, **14**, 2355–2365.
- 22 K. Pradeesh, N. Rao Kotla, S. Ahmad, V. K. Dwivedi and G. V. Prakash, *J. Nanopart.*, 2013, **2013**, 1–13.
- 23 C. Eames, J. M. Frost, P. R. Barnes, B. C. O'Regan, A. Walsh and M. S. Islam, *Nat. Commun.*, 2015, **6**, 7497.
- 24 X. Li, M. I. Dar, C. Yi, J. Luo, M. Tschumi, S. M. Zakeeruddin, M. K. Nazeeruddin, H. Han and M. Gratzel, *Nat. Chem.*, 2015, **7**, 703–711.
- 25 S. Yang, Y. Wang, P. Liu, Y.-B. Cheng, H. J. Zhao and H. G. Yang, *Nat. Energy*, 2016, **1**, 15016.
- 26 Y. Zhao, J. Wei, H. Li, Y. Yan, W. Zhou, D. Yu and Q. Zhao, *Nat. Commun.*, 2016, **7**, 10228.
- 27 H. Fleischer and D. Schollmeyer, *Inorg. Chem.*, 2004, **43**, 5529–5536.
- 28 N. C. Li and R. A. Manning, *J. Am. Chem. Soc.*, 1955, **77**, 5225–5228.
- 29 C. Airoidi and L. N. H. Arakaki, *J. Colloid Interface Sci.*, 2002, **249**, 1–7.
- 30 M. S. Bharara, S. Parkin and D. A. Atwood, *Inorg. Chim. Acta*, 2006, **359**, 3375–3378.
- 31 H. Fleischer, Y. Dienes, B. Mathiasch, V. Schmitt and D. Schollmeyer, *Inorg. Chem.*, 2005, **44**, 8087–8096.
- 32 J. H. Im, C. R. Lee, J. W. Lee, S. W. Park and N. G. Park, *Nanoscale*, 2011, **3**, 4088–4093.
- 33 J.-H. Im, H.-S. Kim and N.-G. Park, *APL Mater.*, 2014, **2**, 081510.
- 34 S. Bae, S. J. Han, T. J. Shin and W. H. Jo, *J. Mater. Chem. A*, 2015, **3**, 23964–23972.
- 35 A. Wakamiya, M. Endo, T. Sasamori, N. Tokitoh, Y. Ogomi, S. Hayase and Y. Murata, *Chem. Lett.*, 2014, **43**, 711–713.
- 36 D. Shen, X. Yu, X. Cai, M. Peng, Y. Ma, X. Su, L. Xiao and D. Zou, *J. Mater. Chem. A*, 2014, **2**, 20454–20461.
- 37 N. Ahn, D. Y. Son, I. H. Jang, S. M. Kang, M. Choi and N. G. Park, *J. Am. Chem. Soc.*, 2015, **137**, 8696–8699.
- 38 Y. Wu, A. Islam, X. Yang, C. Qin, J. Liu, K. Zhang, W. Peng and L. Han, *Energy Environ. Sci.*, 2014, **7**, 2934–2938.
- 39 I. Wharf, T. Gramstad, R. Makhija and M. Onyszczuk, *Can. J. Chem.*, 1976, **54**, 3430–3438.
- 40 J. W. Lee, H. S. Kim and N. G. Park, *Acc. Chem. Res.*, 2016, **49**, 311–319.
- 41 N. J. Jeon, J. H. Noh, Y. C. Kim, W. S. Yang, S. Ryu and S. I. Seok, *Nat. Mater.*, 2014, **13**, 897–903.
- 42 D. P. Nenon, J. A. Christians, L. M. Wheeler, J. L. Blackburn, E. M. Sanehira, B. Dou, M. L. Olsen, K. Zhu, J. J. Berry and J. M. Luther, *Energy Environ. Sci.*, 2016, **9**, 2072–2082.
- 43 Y. Zhao and K. Zhu, *J. Phys. Chem. C*, 2014, **118**, 9412–9418.
- 44 M. Xiao, F. Huang, W. Huang, Y. Dkhissi, Y. Zhu, J. Etheridge, A. Gray-Weale, U. Bach, Y. B. Cheng and L. Spiccia, *Angew. Chem., Int. Ed.*, 2014, **53**, 10056–10061.
- 45 G. J. Li, K. L. Ching, J. Y. L. Ho, M. Wong and H. S. Kwok, *Adv. Energy Mater.*, 2015, **5**, 1401775.
- 46 Y. Chen, M. He, J. Peng, Y. Sun and Z. Liang, *Adv. Sci.*, 2016, **3**, 1500392.
- 47 P. W. Liang, C. Y. Liao, C. C. Chueh, F. Zuo, S. T. Williams, X. K. Xin, J. Lin and A. K. Jen, *Adv. Mater.*, 2014, **26**, 3748–3754.
- 48 Y. Chen, Y. Zhao and Z. Liang, *Chem. Mater.*, 2015, **27**, 1448–1451.
- 49 Z. M. Zhou, Z. W. Wang, Y. Y. Zhou, S. P. Pang, D. Wang, H. X. Xu, Z. H. Liu, N. P. Padture and G. L. Cui, *Angew. Chem., Int. Ed.*, 2015, **54**, 9705–9709.
- 50 Y. Tian and I. G. Scheblykin, *J. Phys. Chem. Lett.*, 2015, **6**, 3466–3470.
- 51 Q. Guo, C. Li, W. Qiao, S. Ma, F. Wang, B. Zhang, L. Hu, S. Dai and Z. a. Tan, *Energy Environ. Sci.*, 2016, **9**, 1486–1494.
- 52 A. Dualeh, P. Gao, S. I. Seok, M. K. Nazeeruddin and M. Grätzel, *Chem. Mater.*, 2014, **26**, 6160–6164.
- 53 T. Baikie, Y. Fang, J. M. Kadro, M. Schreyer, F. Wei, S. G. Mhaisalkar, M. Graetzel and T. J. White, *J. Mater. Chem. A*, 2013, **1**, 5628–5641.
- 54 C. C. Stoumpos, C. D. Malliakas and M. G. Kanatzidis, *Inorg. Chem.*, 2013, **52**, 9019–9038.

